Thermo-mechanical ball bonding simulation with elasto-plastic parameters obtained from nanoindentation and atomic force measurements

A. Wright[1], S. Koffel[1], S.Kraft[1], P. Pichler[1,2], J. Cambieri[3], R. Minixhofer[3] and E. Wachmann[3]
[1]Fraunhofer Institute for Integrated Systems and Device Technology IISB, Erlangen, Germany
[2]Chair of Electron Devices, University of Erlangen-Nuremberg, Erlangen, Germany
[3] ams AG, Unterpremstätten, Austria

Abstract

A ball bonding process was simulated over a high-voltage isolation structure. The removal of an inter-dielectric metal crack-stop layer was investigated through 3D simulation. Material properties for the bonded gold ball were obtained using nanoindentation and atomic force microscopy with a methodology from the work of Ma et al. This yielded both elastic and plastic material parameters. The methodology was then evaluated by using the parameters in a nanoindentation simulation. Although the topography simulated only roughly agreed with measurement, the simulated and measured indenter curves closely overlapped. The parameters were then used in the bonding simulation. The deformation of the bond ball was also measured so that the equivalent deformation could be simulated. This was achieved following the incorporation of both ultrasonic motion and softening in the simulation. Two bonding process geometries were then set up: one with the crack-stop layer present and the other without. Both were simulated and the output was applied within a failure theory to evaluate the risk to the isolation oxide.

1. Introduction

Despite the rise of other technologies such as flip chip and wafer level packaging, wire bonding is still the most commonly used form of interconnection from chip dies to lead frames. A ball bonding process over a high-voltage isolation structure induces high stresses into the underlying dielectric layers through applied force and ultrasonic agitation. Such high stresses may manifest themselves in the formation of cracks which could lead to electrical breakdown at lower voltages than designed. The structure studied in this paper is shown in Figures 1-3. In these, the bonding tool, ball, pad and isolation structure below can be seen. Importantly, a metal layer is present between the upper and lower oxide layers, see Figure 3. The purpose of this layer is to provide a crack stop to prevent any cracks which may form in the upper dielectric traversing to the lower. However, in the interest of increasing the electrical separation between the substrate and bond pad, the question arose whether or not it was feasible to remove this metal layer without unacceptable risk of oxide cracking. One aim of this study was to answer this question through the use of 3D simulation of a bonding process over the structure.

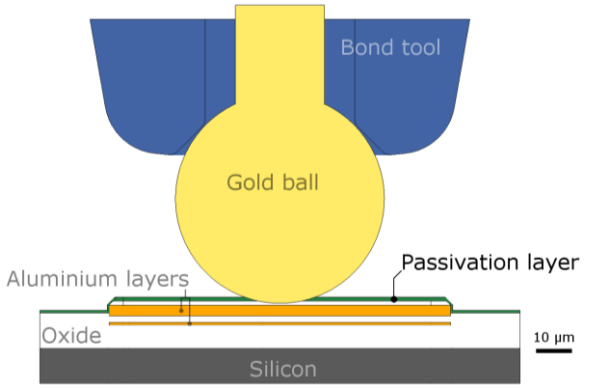

Figure 1: High-voltage isolation structure bonding process model

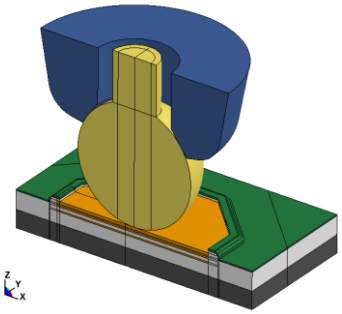

Figure 2: 3D view showing half model with pad layout and passivation coverage.

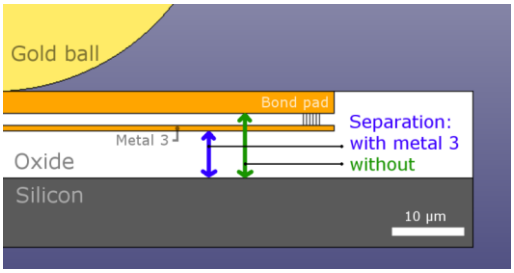

Figure 3: Electrical separation between bond pad and silicon substrate with and without interoxide metal layer.

Very important to any mechanical simulation are adequate parameters for the materials to be simulated. In particular the gold bonding ball has different mechanical properties than the source wire [1] as larger metal grains form while the wire is melted into a ball.

This is the post-print version of the original article published in the proceedings of the
2015 16th International Conference on Thermal, Mechanical and Multi-Physics Simulation and Experiments in Microelectronics and Microsystems (EuroSimE)
which can be found at IEEEXplore (http://dx.doi.org/10.1109/EuroSimE.2015.7103157) © 2015 IEEE

As such, the bonded ball's specific elastic and plastic properties were unknown. For such small objects, nanoindentation readily recovers the Young's modulus. However, parameters of plasticity are also required for reliable simulations. These were obtained from applying a methodology developed by Ma et al. [2] based on both nanoindentation and atomic force microscopy measurements of the indented area. Once the parameters were obtained, they were evaluated by using them in a nanoindentation simulation with the FEM solver LS-Dyna. The results of which were then compared to measurement.

The next aim was to measure the ball deformation in order to simulate it equivalently. This was considered crucial as the bonding ball is the object in the process that transfers the forces from the bond tool to the substrate. The changes in its form during the process also govern the distribution of forces onto the bond pad. Cross sections were made and the amount of deformation was ascertained from the deformed ball height.

To simulate the ball bonding process, LS-Dyna was used again as it is especially capable of simulating large rapid deformation and therefore well suited to wire bonding simulations [3]. Ultrasonic motion and softening were incorporated into the simulation. Sixty cycles of side-to-side motion were included as a high number were found to be necessary to adequately describe the dynamic rate of ball deformation in [4]. Ultrasonic softening was then included to calibrate the amount of deformation.

With the simulation model calibrated, simulations were then carried out to answer the question of whether the crack stop metal layer could be safely removed. The stresses simulated dynamically were then used with a failure theory from Christensen [5] to evaluate the probability of the rupture of the isolation oxide.

2. Obtaining plastic material parameters from nanoindentation and AFM data

Nanoindentation readily provides measurements of elasticity and hardness without information on plasticity. Attempts to obtain plastic parameters from nanoindentation curves were reported in [6, 7]. However, it was found that multiple parameter sets could be found for one indenter curve [2, 7]. The work of Ma et al. [2] avoids this by adding topographic information of the indent to produce a possibly unique set of parameters for an indent curve.

To measure the material properties of a bonded gold ball, a production sample with bonded balls was cross sectioned. This was then measured in a nanoindenter. Indents were made with a Berkovich type indenter tip to a depth of 1 micron. The resultant load on the indenter tip vs. penetration depth is shown in Figure 4. The indent and surrounding surface was then scanned using AFM, see Figure 5. The indent in question is 'a'. Note that the outline of the upper part of the bonded ball can be seen. The AFM was set to scan an area somewhat larger and wider than the indent to capture not only the indent but also the original surface height beyond the extent of any pile-up of the gold.

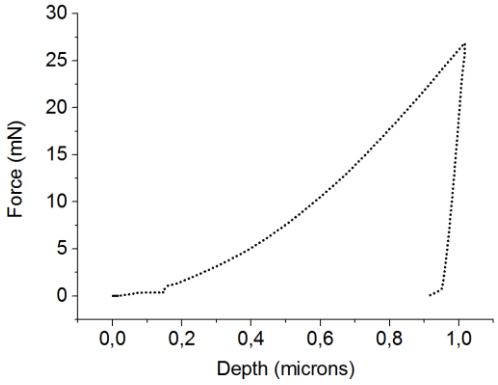

Figure 4: Load on nanoindenter tip versus depth of tip into the bonded gold ball.

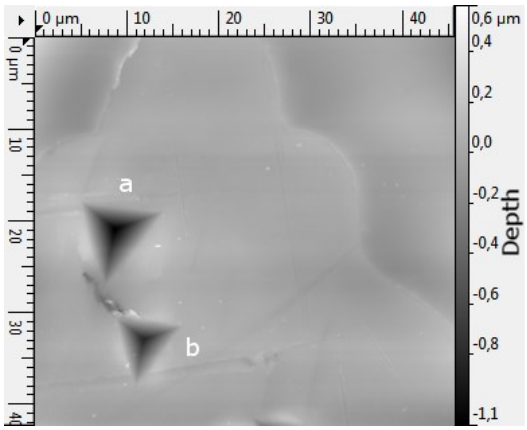

Figure 5: AFM scan of the cross-sectioned gold ball. Indent 'a' to a depth of 1 micron was considered.

When an indent is made in a given material, the material may pile up around the indent as shown in Figure 6, or even sink in. The amount of pile-up (or sink-in) varies across materials, and allows differentiation between material parameters that otherwise yield the same load vs. depth indent curve. In this work, the material exhibited pile-up. To gauge this, the cross-sectional area of the piled up material was compared to that of the cross sectional area of the indent up to the height of the original surface height. These are shown in Figure 6 as the turquoise and blue areas respectively. The AFM image in Figure 5 was cropped to contain only indent 'a'. Rotating the 3D image to a profile view along the white line in Figure 5 yields the image in Figure 7. Note the piling up of material surrounding the indent.

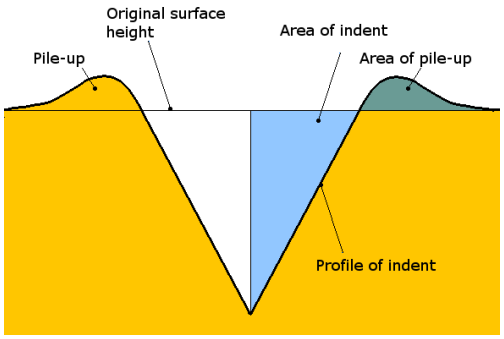

Figure 6: Schematic showing an indent with material pile-up response. The area of the pile-up is shown (turquoise) and the area of the indent (blue) up to the original surface height.

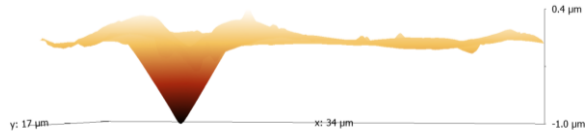

Figure 7: Cross-section of indent topography from AFM. The pile-up can be seen as the material pushed up around the top of the indent.

The methodology of Ma et al. is based on three dimensionless functions that relate parameters from both the indenter curve and the indent cross sectional areas of indent & pile-up to that of Young's modulus, yield strength and strain hardening exponent. Details the procedure can be found in [2]. From the AFM data the cross sectional areas yielded an area ratio of 0.27 of the pile-up area over the indent area. With all necessary parameters, the equations of Ma et al. yielded the mechanical properties of the gold to be:

Young's modulus	70.1 GPa
Yield point	143 MPa
Strain hardening exponent	0.20

From these parameters, a stress-strain graph can be generated. For the elastic region:

$$\sigma = E\varepsilon \text{ for } \sigma \leq \sigma_y \quad (1)$$

where σ, E, ε and σ_y are the stress, Young's modulus, strain and yield stress respectively. For stress beyond yield, a power curve relation suitable for most metals [8] was used:

$$\sigma = K\varepsilon^n \text{ for } \sigma \geq \sigma_y \quad (2)$$

where n is the strain hardening exponent and $K \equiv \sigma_y \left(\frac{E}{\sigma_y}\right)^n$ is the work hardening rate. The resultant stress versus strain curve can be seen in Figure 8.

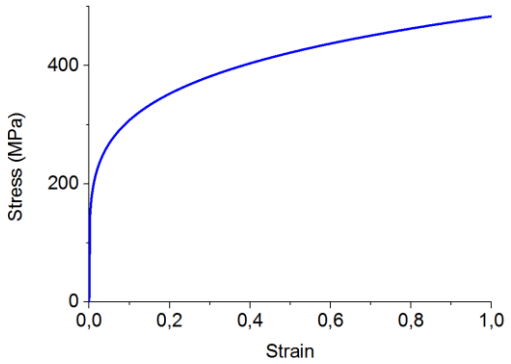

Figure 8: Stress versus strain for the calculated mechanical properties of the bonded gold ball

It was decided to evaluate the obtained parameters by simulating a nanoindentation measurement with the parameters assigned to the material to be indented. To set-up the simulation, the geometry for a Berkovich indenter was constructed and then set to indent a gold substrate to a depth of 1 micron. To save computational resources, the simulated geometry was set-up mirror-symmetrically so that only half of the structure was simulated. The simulated volume was 6×24×2 µm, for the height, the length along symmetry plane and the width, respectively. The material model MAT_106 was used in LS-Dyna with Young's modulus and yield strength given as parameters, and the plastic strain curve via a table. The simulation post indentation is shown in Figure 9.

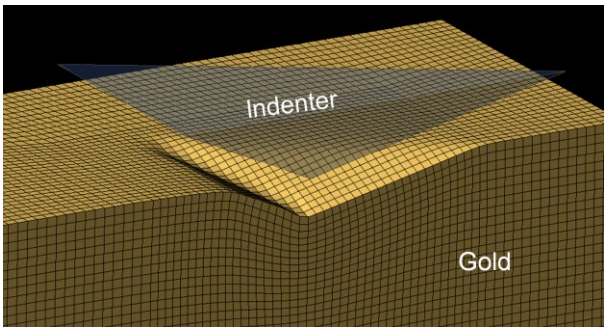

Figure 9: Nanoindentation simulation based on the material parameters of the gold obtained through the methodology of Ma et al.

The resultant load vs. displacement curve on the simulated indenter is shown in Figure 10 alongside that of the measurement. The simulated force vs. depth appears to overlap fairly closely that of the measurement. The topographies of the simulated and a representative measured curve compared in Figure 11 are in reasonable agreement. In the simulation, a smaller pile-up was found than in the measured topography. Part of this discrepancy might be attributed to the indentation which was not exactly perpendicular to the surface. Further uncertainties are introduced by the reduction of the three-dimensional

topography in and around the pyramidal imprint to cross-sectional areas which is not as straight-forward as for a conical indentation tip. However, given the close overlap of the simulated and measured indenter curves, it was decided to use these obtained parameters in the bonding simulation.

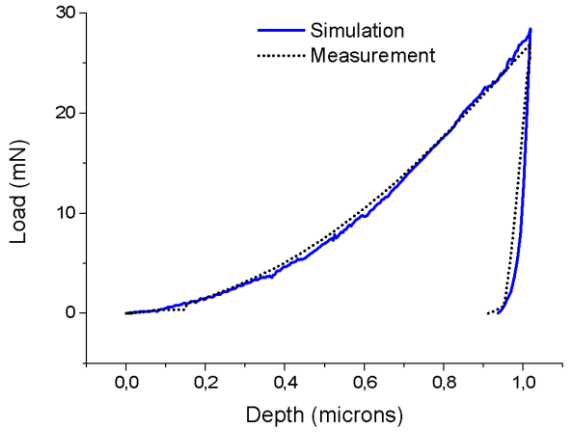

Figure 10: Load on nanoindenter tip versus depth of tip into the bonded gold ball, measurement (black dotted) and from simulation (blue).

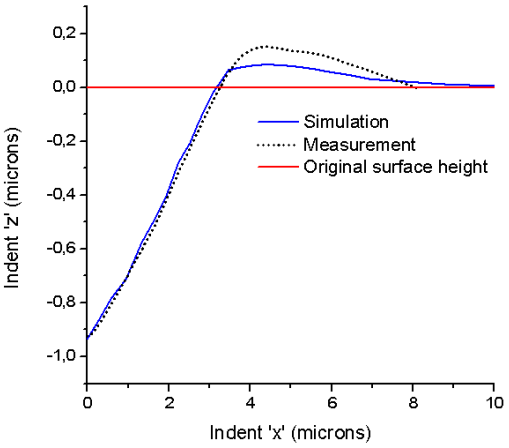

Figure 11: Topography of indents: measured (black dotted) and simulated (blue). Pile up can be seen above the original surface height (red dashed). The measured profile was taken along the dotted white line seen in Figure 5

3. Measuring the amount of deformation to be modelled

The next step was to determine the amount of deformation of the ball during bonding. The height of the deformed ball from its base to the lowest impression of the bond tool (see Figure 12) was taken as the target parameter. Cross sections were made for optical microscopy, Figure 12, and by focused ion beam (FIB) preparation for scanning electron microscopy (SEM) imaging, Figure 13.

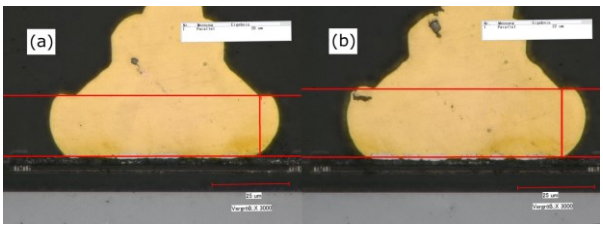

Figure 12: Cross sections of two bonded balls. The deformed ball height, from ball base to the lowest point of the bond tool impression is shown by the horizontal red lines. Deformed ball heights are (a) 20 µm and (b) 22 µm.

The ball heights for the two samples measured from optical micrographs were 20 µm and 22 µm respectively. 20 µm was measured from the FIB cross section. For further modelling, a target deformed ball height of 20 µm was assumed.

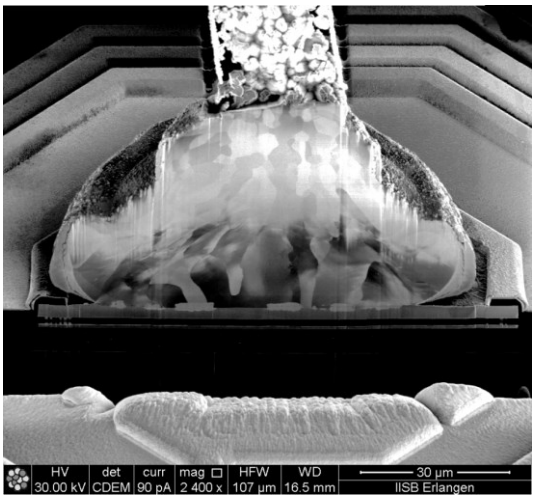

Figure 13: Cross section of bonded ball over isolation structure made by FIB preparation and imaged with SEM.

Additionally, the form of the bond tool's tip could also be reproduced from the cross sections, from the imprint it left upon the bonded ball. This is important as the form affects the force per unit area impinging upon the ball and, hence, through it into the structure. A more accurate initial diameter for the ball was also obtained from the cross sectional area.

4. Simulation model setup

The arrangement of the simulation geometry can be seen in Figure 1 and Figure 2. The simulated structure, including the octagonal bonding pad, was set-up mirror-symmetrically with the symmetry plane being defined by the plane of movement of the capillary. For the sake of a reduction of the computational resources required, only half of the structure was simulated and an appropriate boundary condition added. Nodes were fixed beneath the layer structure along with appropriate boundaries along the outer sides to prevent expansion. All bodies in the model are deformable with the

exception of the top surface of the bond tool which is rigid. During both the impact and bonding stages, a force of 0.6 N acted on the capillary. For the amplitude of the ultrasonic oscillation of the capillary tip, a value of 750 nm was adopted from the laser measurements of Zhong and Goh [9]. For further details on the simulation setup including force ramping, time-scaling and for all material parameters other than gold please refer to [4].

5. Incorporating effects of ultrasonic agitation

The application of ultrasound to the bonding tool imparts both rapid motion to the bonding ball and softens the metal. The simulation was set-up to incorporate 60 cycles of ultrasonic motion which was found necessary to correctly describe evolution of the ball height, see Figure 14. Further information on this setup can be found in [4].

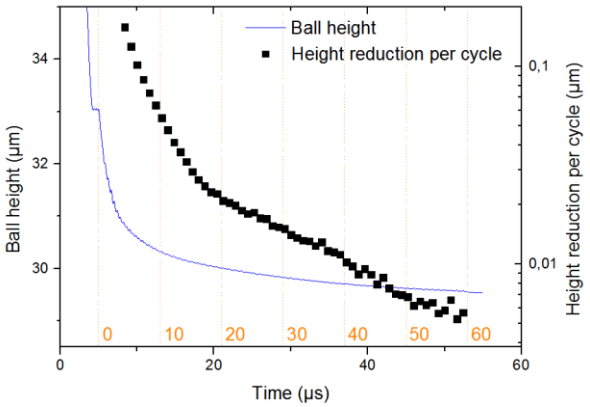

Figure 14: Simulated evolution of the height of the bonding ball during ultrasonic agitation for over 60 cycles. The numbers of cycles are indicated by number and dashed lines.

Simulations carried out with only the ultrasonic motion resulted in a deformed ball height of 29 µm, see Figure 15. However, a further 9 µm is required to match the measured bonded ball.

Next, the phenomenon of ultrasonic softening was incorporated into the simulation. This was used to calibrate the simulated deformed ball height to that of measurement. Ultrasound has the property of softening metals as first described in [10] and reported in experiments by [11–14]. Experiments reported by Langenecker [11] showed that ultrasound with an energy density of 50 W/cm^2 causes at room temperature a similar softening of aluminium as an applied temperature of 600 °C. The stark difference was that only 1/10^7 of the energy was required. The effect was found to be immediate upon the onset of ultrasonic vibration [14]. Frictional heat generated by the ultrasonic motion can be discarded as the source of softening as embedded sensors yielded a temperature rise of only a few degrees during bonding [15, 16], and measurements in [11] showed a delay of 100 ms for a 100 K temperature rise whereas a typical bonding process lasts only 10 ms. Instead, the effect of softening is thought to be from absorption only at defects such as grain boundaries within the metal [17]. Because of the much smaller energy induced and the comparatively small temperature increase measured during bonding, it was assumed that thermal expansion is negligible during the bonding process. Conveniently, ultrasonic softening could then be simulated as thermal softening without expansion.

The thermal softening parameters for gold (bonding ball) and aluminum (bond pad) were adapted from the work of Köster [18] for reduction in Young's modulus with temperature; Ball [19] and Gallagher [20] for the reduction of the yield stress for aluminium and gold respectively; and Liu et al. [21] for changes in plastic strain hardening. With the temperature-dependent parameters for the gold and aluminum adopted from the above sources, simulations with thermal softening at 500 °C resulted in the target deformed ball height being achieved, see Figure 16.

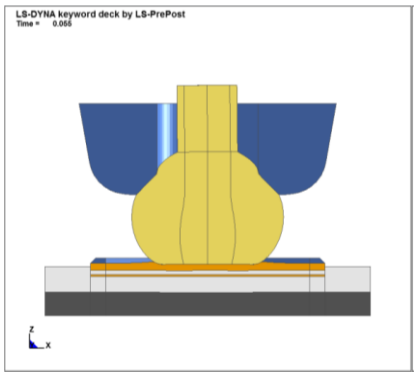

Figure 15: Deformed ball after application of 60 cycles of side-to-side motion. Deformed ball height is 29 µm.

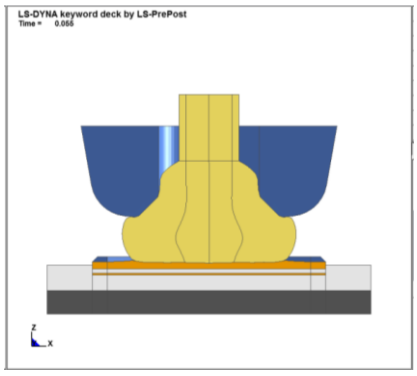

Figure 16: Deformed ball after application of motion and ultrasonic softening, target deformed ball height of 20 µm achieved.

6. Incorporating the effect of bond formation by changing ball to pad friction.

During the bonding process, the ball becomes more and more welded to the pad. This alters the relative sliding of the ball against the pad over time. The amplitude of this relative sliding was measured during a bonding process by Shah et al. [22]. For the simulations in this work, changing the friction between the ball and pad was limited to stepwise changes due to the implementation of contact definitions in LS-Dyna. The stepwise changes to the dynamic friction coefficient were performed over equal intervals between 21 µs to 30 µs from 0.5 via values of 0.8, 1.2 and 1.6 to the maximum of 2.0. The times and values were chosen to follow the proportional change in relative sliding amplitude as that measured by Shah et al. [22]. The resultant relative sliding can be seen in Figure 17. For further information refer to [4].

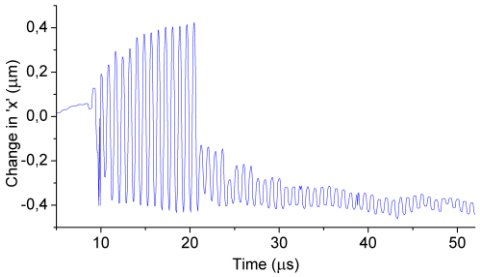

Figure 17: Relative sliding of the centre of the ball against the bonding pad.

7. Simulation of the geometry with and without the crack-stop layer

To assess the effect of the inter-dielectric layer's presence on the risk of isolation failure, two geometries were simulated, one with the inter-dielectric metal layer present, the other without. Removal in the second structure was done by assigning it as dielectric – thus leaving a continuous dielectric layer from bond pad to substrate. For both simulation models, the same mesh was used. The resultant simulated first principal stress can be seen in Figure 18 for the structure with the metal layer present and in Figure 19 without.

It can be seen that there is less overall stress in the structure without the inter-dielectric layer. However, a more thorough consideration is needed to determine whether or not cracks would form in the thick isolation layer from the stresses induced. Therefore, the simulated stresses were assessed within a failure prediction theory.

8. Failure Prediction

For the occurrence of failure for brittle materials, fracture occurs when the maximum principal stress exceeds the ultimate tensile strength σ_{UT} of the material. The above statement holds true for certain conditions of applied stress, however brittle materials

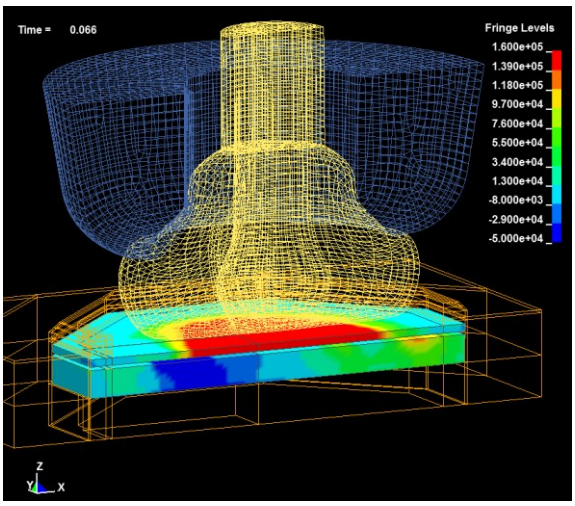

Figure 18: Stress in the dielectric layers for the geometry with the metal crack-stop layer present. A high amount of stress can be seen in the upper isolation layer.

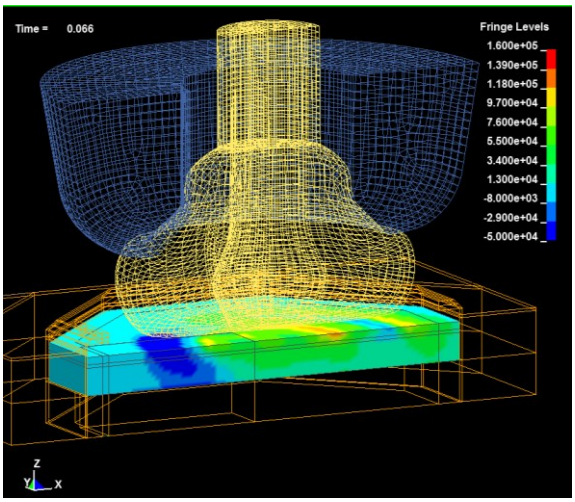

Figure 19: Stress in the continuous thick dielectric layer, metal layer not present. The overall stress appears lower in this case with the metal layer removed.

can already fail from a lower amount of maximum principal stress by the combined effect of perpendicular stresses. This is incorporated into a criterion of failure for materials from the work of Christensen [5]. Christensen's failure theory is encompassed by two failure criteria, where the failure of the material is determined when any one of these are met. Criterion 1,

$$\frac{\sigma_1}{\sigma_{UT}} \leq 1,$$

is the conventional criterion with σ_1 denoting the maximum principal stress. Criterion 2,

$$\left(\frac{1}{\sigma_{UT}} - \frac{1}{\sigma_{UC}}\right)(\sigma_{11} + \sigma_{22} + \sigma_{33}) + \frac{1}{\sigma_{UT}\sigma_{UC}} \times \{[(\sigma_{11} - \sigma_{22})^2 + (\sigma_{22} - \sigma_{33})^2 + (\sigma_{33} - \sigma_{11})^2]/2 + 3({\sigma_{12}}^2 + {\sigma_{23}}^2 + {\sigma_{31}}^2)\} \leq 1,$$

is a criterion suggested by Christensen with $\sigma_{11}, \sigma_{22}, \sigma_{33}$ denoting the components of the normal stress, σ_{12}, σ_{23}, σ_{31} the components of the shear stress, and σ_{UT} and σ_{UC} the ultimate tensile and compressive strengths of the material, respectively. Values for these ultimate strengths for the SiO_2 dielectric material in the structure were obtained from [23] and [24] as σ_{UT} = 364 MPa and σ_{UC} = 1100 MPa, respectively

The combined failure prediction theory was applied to the modelling results for the thick isolation oxide in both simulations. The resultant failure prediction for both models can be seen in Figure 20.

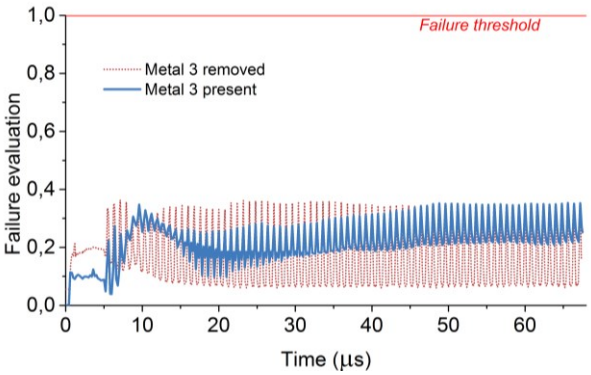

Figure 20: Failure prediction for the high-voltage isolation layer, with the crack stop metal layer (blue) and without (blue)

It can be seen that for both cases, no failure of the isolation layers is predicted. This would suggest that the removal of the inter-dielectric metal layer would be safe.

9. Conclusion

In this work, a ball bonding process was simulated over a high-voltage isolation structure. Elastic and plastic material parameters for the gold ball were obtained through nanoindentation and AFM measurements used with equations from Ma et al. [2]. The obtained parameters were evaluated in a simulation of a nanoindentation measurement. Although the topography did not match, the indenter curves closely overlapped, thus the parameters were used. The amount of deformation of the gold ball was determined through measurement of cross sections made of a production sample. The ultrasonic effects of motion and softening were incorporated into the simulation; the latter calibrated the simulation to model the same amount of deformation as that measured. Additionally, dynamic friction was added to the model to simulate the forming bond.

The study sought to answer the question of whether or not an inter-dielectric metal layer, designed as a crack stop, could be safely removed to extend the electrical separation in the structure. Based on the stress simulated for both cases, combined with the use of a failure theory, this was answered. The structure without crack-stop layer showed no higher probability of failure than that with and it would therefore be safe, from these results, to remove the metal layer.

Acknowledgments

The author would like to acknowledge the assistance of Florian Stumpf for AFM measurements, Susanne Beuer for FIB milling and SEM imaging and Thomas Filippi for optical microscopy and preparation. The research leading to these results has received funding from the European Union Seventh Framework Programme (FP7/2007-2013) under grant agreement n° 285739 (ESTRELIA).

References

[1] Dresbach, C, Lorenz, G, Petzold, M, and Altenbach, H, "Analysis of Chip Damage Risk in Thermosonic Wire Bonding," *KEM*, Vol. 478. (2011), pp. 75–80.

[2] Ma, Z. S, Zhou, Y. C, Long, S. G, Zhong, X. L, and Lu, C, "Characterization of stress-strain relationships of elastoplastic materials: An improved method with conical and pyramidal indenters," *Mechanics of Materials*, Vol. 54. (2012), pp. 113–123.

[3] Kraemer, F. and Wiese, S, "FEM wire bonding simulation for sensor chip applications," in *2014 15th International Conference on Thermal, Mechanical and Multi-Physics Simulation and Experiments in Microelectronics and Microsystems (EuroSimE),* Ghent, Belgium, April. 2014.

[4] Wright, A, Koffel, S, Pichler, P, Enichlmair, H, Minixhofer, R, and Wachmann, E, "On the thermo-mechanical modelling of a ball bonding process with ultrasonic softening," in *2013 14th International Conference on Thermal, Mechanical and Multi-Physics Simulation and Experiments in Microelectronics and Microsystems (EuroSimE),* Wroclaw, Poland, April. 2013.

[5] Christensen, R. M, "A Comprehensive Theory of Yielding and Failure for Isotropic Materials," *J. Eng. Mater. Technol,* Vol. 129, No. 2. (2007), p. 173.

[6] Dao, M, Chollacoop, N, van Vliet, K, Venkatesh, T, and Suresh, S, "Computational modeling of the forward and reverse problems in instrumented sharp indentation," *Acta Materialia*, Vol. 49, No. 19. (2001), pp. 3899–3918.

[7] Casals, O. and Alcalá, J, "The duality in mechanical property extractions from Vickers and Berkovich instrumented indentation experiments," *Acta Materialia*, Vol. 53, No. 13. (2005), pp. 3545–3561.

[8] A.S.M. International, Atlas of Stress-strain Curves (2002), p. 6.

[9] Zhong, Z. and Goh, K, "Investigation of ultrasonic vibrations of wire-bonding capillaries," *Microelectronics Journal*, Vol. 37, No. 2. (2006), pp. 107–113.

[10] Blaha, F. and Langenecker, B, "Dehnung von Zink-Kristallen unter Ultraschalleinwirkung," *Naturwissenschaften*, Vol. 42, No. 20. (1955), p. 556.

[11] Langenecker, B, "Effects of ultrasound on deformation characteristics of metals," *IEEE Transactions on Sonics and Ultrasonics*, Vol. 13, No. 1. (1966), pp. 1–88.

[12] Lum, I, Huang, H, Chang, B. H, Mayer, M, Du, D, and Zhou, Y, "Effects of superimposed ultrasound on deformation of gold," *J. Appl. Phys,* Vol. 105, No. 2. (2009), p. 24905.

[13] Daud, Y, Lucas, M, and Huang, Z, "Modelling the effects of superimposed ultrasonic vibrations on tension and compression tests of aluminium," *Journal of Materials Processing Technology*, Vol. 186, No. 1-3. (2007), pp. 179–190.

[14] Yao, Z, Kim, G.-Y, Wang, Z, Faidley, L, Zou, Q, Mei, D, and Chen, Z, "Acoustic softening and residual hardening in aluminum: Modeling and experiments," *International Journal of Plasticity*, Vol. 39. (2012), pp. 75–87.

[15] Mayer, M, Paul, O, Bolliger, D, and Baltes, H, "Integrated temperature microsensors for characterization and optimization of thermosonic ball bonding process," *IEEE Trans. Comp. Packag. Technol,* Vol. 23, No. 2. (2000), pp. 393–398.

[16] Suman, S, Gaitan, M, Joshi, Y, and Harman, G, "Wire-bonding process monitoring using thermopile temperature sensor," *IEEE Trans. Adv. Packag,* Vol. 28, No. 4. (2005), pp. 685–693.

[17] Siddiq, A. and El Sayed, T, "Ultrasonic-assisted manufacturing processes: Variational model and numerical simulations," *Ultrasonics*, Vol. 52, No. 4. (2012), pp. 521–529.

[18] Köster, W, "Die Temperaturabhängigkeit des Elastizitätsmoduls reiner Metalle," *Zeitschrift für Metallkunde*, Vol. 39, No. 1. (1948), pp. 1–9.

[19] Ball, C. J, "The flow stress of polycrystalline aluminium," *Philosophical Magazine*, Vol. 2, No. 20. (1957), pp. 1011–1017.

[20] Gallagher, P. C. J, "The high temperature flow stress of single crystals of copper, silver and gold. Part I," *Philosophical Magazine*, Vol. 15, No. 133. (1967), pp. 51–83.

[21] Liu, D, Tsai, C, and Lzu, S, "Determination of temperature-dependent elasto-plastic properties of thin-film by MD nanoindentation simulations and an inverse GA/FEM computational scheme," *Computers, Materials and Continua*, Vol. 11, No. 2. (2009), pp. 147–164.

[22] Shah, A, Mayer, M, Qin, I, Huynh, C, Zhou, Y, and Meyer, M, "Ultrasonic friction power during thermosonic Au and Cu ball bonding," *J. Phys. D: Appl. Phys,* Vol. 43, No. 32. (2010), p. 325301.

[23] Sharpe, W. N, Pulskamp, J, Gianola, D. S, Eberl, C, Polcawich, R. G, and Thompson, R. J, "Strain Measurements of Silicon Dioxide Microspecimens by Digital Imaging Processing," *Exp Mech*, Vol. 47, No. 5. (2007), pp. 649–658.

[24] Vass, C, Smausz, T, and Hopp, B, "Wet etching of fused silica: a multiplex study," *J. Phys. D: Appl. Phys,* Vol. 37, No. 17. (2004), pp. 2449–2454.